View metadata, citation and similar papers at core.ac.uk
brought to you by CORE
provided by Caltech Authors

Supplementary Material: Phonon Collapse and Second-Order Phase Transition in Thermoelectric SnSe

Unai Aseginolaza[1,2,3], Raffaello Bianco[4,5,6], Lorenzo Monacelli[4], Lorenzo Paulatto[7], Matteo Calandra[8], Francesco Mauri[4,5], Aitor Bergara[1,2,9], and Ion Errea[2,3]

[1]Centro de Física de Materiales CFM, CSIC-UPV/EHU, Paseo Manuel de Lardizabal 5, 20018 Donostia, Basque Country, Spain
[2]Donostia International Physics Center (DIPC), Manuel Lardizabal pasealekua 4, 20018 Donostia, Basque Country, Spain
[3]Fisika Aplikatua 1 Saila, University of the Basque Country (UPV/EHU), Europa Plaza 1, 20018 Donostia, Basque Country, Spain
[4]Dipartimento di Fisica, Università di Roma La Sapienza, Piazzale Aldo Moro 5, I-00185 Roma, Italy
[5]Graphene Labs, Fondazione Instituto Italiano di Tecnologia, Italy
[6]Department of Applied Physics and Material Science, Steele Laboratory, California Institute of Technology, Pasadena, California 91125, United States
[7]IMPMC, UMR CNRS 7590, Sorbonne Universités - UPMC Univ. Paris 06, MNHN, IRD, 4 Place Jussieu, F-75005 Paris, France
[8]Sorbonne Universités, CNRS, Institut des Nanosciences de Paris, UMR7588, F-75252, Paris, France
[9]Departamento de Física de la Materia Condensada, University of the Basque Country (UPV/EHU), 48080 Bilbao, Basque Country, Spain

1 Structure and high symmetry points

The *Cmcm* and *Pnma* phases are orthorhombic and their structure is shown in the main text. The *Cmcm* phase has a centering in the XZ plane of the rectangular conventional cell and contains 4 atoms in the primitive cell. The primitive cell of the *Pnma* phase is the conventional cell and contains 8 atoms. The primitive lattice vectors of the *Cmcm* structure are: $\mathbf{a}_1 = (a/2, 0, c/2)$, $\mathbf{a}_2 = (-a/2, 0, c/2)$ and $\mathbf{a}_3 = (0, b, 0)$, where a (long axis), b and c are the lattice constants of the conventional cell.

Symmetry point	Reduced **q** vector
Z	0.0, 0.0, 0.5
R	0.0, 0.5, 0.5
S	0.0, 0.5, 0.0
Γ	0.0, 0.0, 0.0
Y	0.5, -0.5, 0.0
T	0.5, 0.5, 0.5

Table 1: Reduced **q** vectors of the high symmetry points in the Brillouin zone of the $Cmcm$ phase. The coordinates are given with respect to the reciprocal lattice vectors of the primitive cell.

The atomic positions (x, y, z in crystal units) in the $Cmcm$ phase belong to the 4c Wyckoff position and at 700 and 800 K for LDA are the following:
Sn (T=700 K) 0.1250893457 0.0 0.5
Se (T=700 K) 0.3591529376 0.0 0.5
Sn (T=800 K) 0.1254334803 0.0 0.5
Se (T=800 K) 0.3593533288 0.0 0.5
They are basically the same at the temperatures used in the main text, because the only degree of freedom is in the x direction. The reciprocal lattice vectors of the $Cmcm$ primitive first Brillouin zone are $\mathbf{b}_1 = 2\pi(1/a, 0, 1/c)$, $\mathbf{b}_2 = 2\pi(-1/a, 0, 1/c)$ and $\mathbf{b}_3 = 2\pi(0, 1/b, 0)$. The high symmetry points and their coordinates used in phonon dispersion figures are listed in table 1.

2 Calculation methods, pseudopotentials and parameters

Our calculations are based on Density Functional Theory (DFT) using the QUANTUM-ESPRESSO[1] software package and pseudopotentials taken from its web page. Harmonic phonons were calculated within Density Functional Perturbation Theory[2] and perturbative third-order force-constants (TOFC) were calculated within Density Functional Pertubation Theory[3] (DFPT) or finite differences[4]. Anharmonic phonons and non-perturbative TOFCs were calculated using the SSCHA. For the exchange-correlation interaction we use the Perdew-Burke-Ernzerhof[5] (PBE) generalized gradient approximation and the local density approximation (LDA) with ultrasoft[6] (US) and Projector Augmented Wave method[7] (PAW) pseudopotentials respectively. Due to limitations in the implementation of perturbative TOFCs within DFPT we use norm-conserving (NC) pseudopotentials[8] and finite differences within PBE. In the LDA case we can see the comparison with the PAW pseudopotential (using a finite difference approach[4]) for the thermal conductivity in Fig. 1. We also include the calculation with effective charges in the phonon spectrum, as we can see, the difference is negligible. The calculation beyond the Single Mode Approximation (SMA) (the iterative method[9]) is also included. As it is expected for high temperatures, the effect is small. The thermal conductivity in the fully relaxed structure is also included, as we can see the volume effect is small. We use a cutoff energy of 70 Ry and a grid of $16 \times 16 \times 16$ **K** points to sample the first Brillouin zone. For the harmonic phonon calculations we use a $6 \times 6 \times 6$ supercell and a $2 \times 2 \times 2$ one for the TOFCs. The convergence

of the TOFCs is tested in the thermal conductivity with a $4 \times 4 \times 4$ supercell in Fig. 1 and the difference is small. For the SSCHA calculation we use a $2 \times 2 \times 2$ supercell. Then, for the phonon dispersion, we interpolate the difference between the harmonic and anharmonic force-constants in the $2 \times 2 \times 2$ supercell to the $6 \times 6 \times 6$ and we add it to the $6 \times 6 \times 6$ harmonic force constants. For the linewidth calculations we use a $20 \times 20 \times 20$ $\mathbf{q}$ points grid obtained by Fourier interpolation with a smearing of 1 cm^{-1}. For the thermal conductivity calculation we use a $10 \times 10 \times 10$ grid of $\mathbf{q}$ points to sample the first Brillouin zone. We have done calculations in denser grids to test these parameters.

3 Volume effects in the harmonic phonon spectrum

In this section we will analyze the volume effects in the harmonic phonon spectrum of *Cmcm* SnSe. In Fig. 2 we can see the LDA and PBE phonon spectra in the theoretical and experimental structures. As we can see, within LDA, the difference between phonons in the theoretical and experimental structures is clearly visible. Due to the bigger volume in the experimental cell, there is a red shift of almost all the vibrational modes and furthermore, more imaginary frequencies arise at the Γ and Y points. Within PBE, the phonon spectra in the theoretical and experimental structures are much more similar, because the lattice parameters in these structures are very similar as well. These results are in agreement with our T_c calculations shown in the main text, where T_c is basically the same in the two structures within PBE and completely different within LDA. We conclude that the harmonic phonons of SnSe are very sensitive to the volume of the unit cell.

In order to compare with the calculations in Ref. [10] and see whether the change from $c/b > 1$ to $c/b < 1$ is responsible for creating the instability at the point Y, we have done the phonon calculation using the lattice parameters of Ref. [10]. The result is shown in Fig. 3. It is clear that the change in the lattice parameters does not alter the instability, as expected for such a small change.

4 Anharmonic theory: SSCHA

We study the lattice dynamics of SnSe in the Born-Oppenheimer (BO) approximation, thus we consider the quantum Hamiltonian for the atoms defined by the BO potential energy $V(\mathbf{R})$. With $\mathbf{R}$ we are denoting in component-free notation the quantity $R^{s\alpha}(\mathbf{l})$, which is a collective coordinate that completely specifies the atomic configuration of the crystal. The index α denotes the Cartesian direction, s labels the atom within the unit cell and $\mathbf{l}$ indicates the three dimensional lattice vector. In what follows we will also use a single composite index $a = (\alpha, s, \mathbf{l})$ to indicate Cartesian index α, atom s index and lattice vector $\mathbf{l}$. Moreover, in general, we will use bold letters to indicate also other quantities in component-free notation.

In order to take into account quantum effects and anharmonicity at a non-perturbative level, we use the Stochastic Self-Consistent Harmonic Approximation (SSCHA). For a given temperature T, the method allows to find an approximation for $F(\boldsymbol{\mathcal{R}})$, the free energy of the crystal as a function of the average atomic position $\mathcal{R}^a$ (the centroids). For a given centroid $\boldsymbol{\mathcal{R}}$, the SSCHA free energy is obtained through an auxiliary quadratic Hamiltonian, the SSCHA Hamiltonian $\mathcal{H}_{\boldsymbol{\mathcal{R}}}$. In a displacive second-order phase transition, at high temperature the free

energy has a minimum in a high symmetry configuration $\boldsymbol{\mathcal{R}}_{hs}$ but, on lowering temperature, $\boldsymbol{\mathcal{R}}_{hs}$ becomes a saddle point at the transition temperature T_c. Therefore, the free energy Hessian evaluated in $\boldsymbol{\mathcal{R}}_{hs}$, $\partial^2 F/\partial\boldsymbol{\mathcal{R}}\partial\boldsymbol{\mathcal{R}}|_{\boldsymbol{\mathcal{R}}_{hs}}$, at high temperature is positive definite but it develops one or multiple negative eigendirections at T_c. The SSCHA free energy Hessian can be computed by using the analytic formula (in component-free notation)

$$\frac{\partial^2 F}{\partial\boldsymbol{\mathcal{R}}\partial\boldsymbol{\mathcal{R}}} = \boldsymbol{\Phi} + \overset{(3)}{\boldsymbol{\Phi}}\boldsymbol{\Lambda}(0)[\mathbf{1} - \overset{(4)}{\boldsymbol{\Phi}}\boldsymbol{\Lambda}(0)]^{-1}\overset{(3)}{\boldsymbol{\Phi}}, \tag{1}$$

with

$$\boldsymbol{\Phi} = \left\langle \frac{\partial^2 V}{\partial\mathbf{R}\partial\mathbf{R}} \right\rangle_{\rho_{\mathcal{H}_\mathcal{R}}}, \overset{(3)}{\boldsymbol{\Phi}} = \left\langle \frac{\partial^3 V}{\partial\mathbf{R}\partial\mathbf{R}\partial\mathbf{R}} \right\rangle_{\rho_{\mathcal{H}_\mathcal{R}}}, \overset{(4)}{\boldsymbol{\Phi}} = \left\langle \frac{\partial^4 V}{\partial\mathbf{R}\partial\mathbf{R}\partial\mathbf{R}\partial\mathbf{R}} \right\rangle_{\rho_{\mathcal{H}_\mathcal{R}}}, \tag{2}$$

where the averages are with respect to the density matrix of the SSCHA Hamiltonian $\mathcal{H}_\mathcal{R}$. i.e $\rho_{\mathcal{H}_\mathcal{R}} = e^{-\beta\mathcal{H}_\mathcal{R}}/tr[e^{-\beta\mathcal{H}_\mathcal{R}}]$ (labeled as $\rho_{\mathcal{R},\boldsymbol{\Phi}}$ in the main text), and $\beta = (K_B T)^{-1}$ where K_B is the Boltzmann constant. In Eq. 1 the value $z = 0$ of the 4th-order tensor $\boldsymbol{\Lambda}(z)$ is used. For a generic complex number z it is defined, in components, by

$$\Lambda^{abcd}(z) = -\frac{1}{2}\sum_{\mu\nu}\tilde{F}(z,\tilde{\Omega}_\mu,\tilde{\Omega}_\nu) \times \sqrt{\frac{\hbar}{2M_a\tilde{\Omega}_\mu}}e^a_\mu \sqrt{\frac{\hbar}{2M_b\tilde{\Omega}_\nu}}e^b_\nu \sqrt{\frac{\hbar}{2M_c\tilde{\Omega}_\mu}}e^c_\mu \sqrt{\frac{\hbar}{2M_d\tilde{\Omega}_\nu}}e^d_\nu, \tag{3}$$

with M_a the mass of the atom a, $\tilde{\Omega}^2_\mu$ and e^a_μ eigenvalues and corresponding eigenvectors of $D^{(S)}_{ab} = \boldsymbol{\Phi}_{ab}/\sqrt{M_a M_b}$, respectively, and

$$\tilde{F}(z,\tilde{\Omega}_\mu,\tilde{\Omega}_\nu) = \frac{2}{\hbar}\left[\frac{(\tilde{\Omega}_\mu+\tilde{\Omega}_\nu)[1+n_B(\tilde{\Omega}_\mu)+n_B(\tilde{\Omega}_\nu)]}{(\tilde{\Omega}_\mu+\tilde{\Omega}_\nu)^2 - z^2} - \frac{(\tilde{\Omega}_\mu-\tilde{\Omega}_\nu)[n_B(\tilde{\Omega}_\mu)-n_B(\tilde{\Omega}_\nu)]}{(\tilde{\Omega}_\mu-\tilde{\Omega}_\nu)^2 - z^2}\right] \tag{4}$$

where $n_B(\omega) = 1/(e^{\beta\hbar\omega}-1)$ is the bosonic occupation number. Evaluating through Eq. 1 the free energy Hessian in $\boldsymbol{\mathcal{R}}_{hs}$ and studying its spectrum as a function of temperature, we can predict the occurrence of a displacive second-order phase transition and estimate T_c. In particular, since we are considering a crystal, we take advantage of lattice periodicity and we Fourier transform the free energy Hessian with respect to the lattice indexes. Therefore, since there are 4 atoms in the unit cell of SnSe, we actually calculate the eigenvalues of the two dimensional 12×12 square matrix $\partial^2 F/\partial\mathcal{R}^a(-\mathbf{q})\partial\mathcal{R}^b(\mathbf{q})$ in different $\mathbf{q}$ of the Brillouin zone.

As shown in ref. [11], in the context of the SSCHA it is possible to formulate an ansatz in order to give an approximate expression to the one-phonon Green function $\mathbf{G}(z)$ for the variable $\sqrt{M_a}(R^a - \mathcal{R}^a_{hs})$:

$$\mathbf{G}^{-1}(z) = z^2\mathbf{1} - \mathbf{M}^{-\frac{1}{2}}\boldsymbol{\Phi}\mathbf{M}^{-\frac{1}{2}} - \boldsymbol{\Pi}(z), \tag{5}$$

where $\mathbf{G}^{-1}(0) = -\mathbf{D}^{(F)}$, $D^{(F)}_{ab} = \frac{1}{\sqrt{M_a M_b}}\frac{\partial^2 F}{\partial\mathcal{R}_a\partial\mathcal{R}_b}$, and $\Pi(z)$ is the SSCHA self-energy, given by

$$\Pi(z) = \mathbf{M}^{-\frac{1}{2}}\overset{(3)}{\boldsymbol{\Phi}}\boldsymbol{\Lambda}(z)[\mathbf{1} - \overset{(4)}{\boldsymbol{\Phi}}\boldsymbol{\Lambda}(z)]^{-1}\overset{(3)}{\boldsymbol{\Phi}}\mathbf{M}^{-\frac{1}{2}}, \tag{6}$$

where $M_{ab} = \delta_{ab}M_a$ is the mass matrix. As can be seen in Fig. 4, for the applications considered in the present paper, the static term $\overset{(4)}{\boldsymbol{\Phi}}\boldsymbol{\Lambda}(0)$ is negligible with respect to the identity matrix.

We can also see the convergence of the frequencies with respect to the amount of stochastic configurations. Extending this approximation to the dynamical case reduces the SSCHA self-energy to the so called bubble self-energy, namely

$$\mathbf{\Pi} \approx \mathbf{\Pi}^{(B)}(z) = \mathbf{M}^{-\frac{1}{2}} \overset{(3)}{\mathbf{\Phi}} \mathbf{\Lambda}(z) \overset{(3)}{\mathbf{\Phi}} \mathbf{M}^{-\frac{1}{2}}. \tag{7}$$

We then neglect the mixing between different phonon modes and assume that $\mathbf{\Pi}(z)$ is diagonal in the basis of the eigenvectors $e_\mu^a(\mathbf{q})$ of $\Phi_{ab}(\mathbf{q})/\sqrt{M_a M_b}$ where $\Phi_{ab}(\mathbf{q})$ is the Fourier transform of the real space Φ (now a and b represent atoms in the unit cell and Cartesian indices). We then define

$$\Pi_\mu(\mathbf{q}, \omega) = \sum_{a,b} e_\mu^a(-\mathbf{q}) \Pi_{ab}(\mathbf{q}, \omega + i0^+) e_\mu^b(\mathbf{q}). \tag{8}$$

The phonon frequencies squared, $\Omega_\mu^2(\mathbf{q})$, corrected by the bubble self-energy are then obtained as

$$\Omega_\mu^2(\mathbf{q}) = \tilde{\Omega}_\mu^2(\mathbf{q}) + Re\Pi_\mu(\mathbf{q}, \tilde{\Omega}_\mu(\mathbf{q})), \tag{9}$$

where $\tilde{\Omega}_\mu^2(\mathbf{q})$ are the eigenvalues of the Fourier transform of $\mathbf{D}^{(S)}$.

In studying the response of a lattice to neutron scattering we need the one-phonon spectral function. By using Eq. 5 for $\mathbf{G}(z)$ we can calculate the cross-section $\sigma(\omega) = -\omega Tr Im\mathbf{G}(\omega + i0^+)/\pi$, whose peaks signal the presence of collective vibrational excitations (phonons) having certain energies, as they can be probed with inelastic scattering experiments. Again, we take advantage of the lattice periodicity and we Fourier transform the interesting quantities with respect to the lattice indices. In particular, we consider the Fourier transform of the SSCHA self-energy, $\Pi_{ab}(\mathbf{q}, z)$. Neglecting the mixing between different modes, the cross section is then given by

$$\sigma(\mathbf{q}, \omega) = \frac{1}{\pi} \sum_\mu \frac{-\omega Im\Pi_\mu(\mathbf{q}, \omega)}{(\omega^2 - \tilde{\Omega}_\mu^2(\mathbf{q}) - Re\Pi_\mu(\mathbf{q}, \omega))^2 + (Im\Pi_\mu(\mathbf{q}, \omega))^2}. \tag{10}$$

If we neglect the frequency dependence of the phonon self-energy, we get the weakly anharmonic limit of the cross section, which is going to be a sum of Lorentzian functions.

5 SSCHA phonons and spectral functions

In Fig. 5 we compare the harmonic, $\tilde{\Omega}_\mu(\mathbf{q})$ and $\Omega_\mu(\mathbf{q})$ frequencies in order to have an idea of the anharmonic effects. As we can see by looking at the $\tilde{\Omega}_\mu$ frequencies (SCHA second-order force-constants), all the instabilities that appear in the harmonic approximation are suppressed. Then, by comparing the $\tilde{\Omega}_\mu$ and Ω_μ frequencies, we see that the anharmonic third-order produces a red shift of all the modes. Therefore, the contribution of the bubble self-energy term is crucial in this material for all the modes, reflecting the large effect of the TOFCs.

In Fig. 6 we compare the spectral functions calculated with the non-perturbative $\overset{(3)}{\mathbf{\Phi}}$ force-constants and perturbative $\overset{(3)}{\phi}$ force-constants. We also include the spectral functions calculated within the Lorentzian approximation. As we can see, the non-lorentzian shape of the Γ_1, Γ_2, Y_2 and Y_3 modes is increased in the non-perturbative case.

6 Third order force-constants: Centering, acoustic sum rule, stochastic noise and temperature dependence

In this section we summarize how we calculate proper perturbative TOFCs in real space for the Fourier interpolation, which is crucial for calculating the linewidth or the self-energy. In general, for the TOFCs in real and reciprocal space we can use the following notation:

$$\overset{(3)}{\tilde{\phi}}_{abc}(\mathbf{q},\mathbf{q}',\mathbf{q}'') = \frac{1}{N}\frac{\partial^3 V}{\partial u_a(\mathbf{q})\partial u_b(\mathbf{q}')\partial u_c(\mathbf{q}'')}\bigg|_0, \quad \overset{(3)}{\phi}_{abc}(\mathbf{l},\mathbf{l}',\mathbf{l}'') = \frac{\partial^3 V}{\partial u_a(\mathbf{l})\partial u_b(\mathbf{l}')\partial u_c(\mathbf{l}'')}\bigg|_0, \tag{11}$$

where $u_a(\mathbf{l})$ is the displacement of atom a (a accounts also for the Cartesian index) in cell $\mathbf{l}$, $u_a(\mathbf{q})$ its Fourier transform, and N the number of unit cells in the crystal. Within perturbation theory, $\overset{(3)}{\tilde{\boldsymbol{\phi}}}$ matrices are calculated *ab initio* on a uniform grid of $\mathbf{q}$ points centered in the origin, meaning that both vectors $\mathbf{q}'$ and $\mathbf{q}''$ run on the grid, while $\mathbf{q} = -\mathbf{q}' - \mathbf{q}''$. We then define the Fourier interpolation

$$\overset{(3)}{\phi}_{abc}(\mathbf{0},\mathbf{l}',\mathbf{l}'') = \frac{1}{N^2}\sum_{\mathbf{q}',\mathbf{q}''} \overset{(3)}{\tilde{\phi}}_{abc}(\mathbf{q},\mathbf{q}',\mathbf{q}'')e^{-i(\mathbf{q}'\cdot\mathbf{l}'+\mathbf{q}''\cdot\mathbf{l}'')}, \tag{12}$$

where the sums are performed in the grid points. We can set $\mathbf{l} = 0$ because of translational symmetry. TOFCs calculated in this way are named non-centered TOFCs and they are not physically sensible, because they are periodic in real space and do not exponentially decay when the distances among the three atoms increase. Therefore, they are not the best option for the Fourier interpolation. In order to calculate proper TOFCs $\overset{(3)^{cen}}{\boldsymbol{\phi}}$, we apply the following procedure: The force-constants $\overset{(3)}{\phi}_{abc}$ correspond to three atoms at the positions $\boldsymbol{\tau}_a$, $\boldsymbol{\tau}_b + \mathbf{l}'$ and $\boldsymbol{\tau}_c + \mathbf{l}''$, where $\boldsymbol{\tau}_a$ are the atomic position vectors inside the unit cell. The three atoms form a triangle with perimeter $P = |\mathbf{d}_1| + |\mathbf{d}_2| + |\mathbf{d}_3|$, where $\mathbf{d}_1$, $\mathbf{d}_2$, $\mathbf{d}_3$ are the distances among the three atoms. First of all we calculate the perimeter P of the triangle. If P is the shortest perimeter among the perimeters of all the triangles formed by the triplet of atoms supercell equivalent to the original three, we put $\overset{(3)^{cen}}{\phi}_{abc}(\mathbf{0},\mathbf{l}',\mathbf{l}'') = \overset{(3)}{\phi}_{abc}(\mathbf{0},\mathbf{l}',\mathbf{l}'')/N_{eq}$, where N_{eq} is the number of triangles with perimeter equal to P. For larger equivalent perimeters the TOFC is set to 0. This criterion stems from the assumption of a long-range exponential decay of the force-constants and it is named centering. That is why $\overset{(3)^{cen}}{\boldsymbol{\phi}}$ are centered and are optimized for the Fourier interpolation.

We will see now what happens to the sum rules of TOFCs after centering. In general, physical TOFCs fulfill the following sum rule (now we separate again into atom (ijk) and Cartesian ($\alpha\beta\gamma$) indices)

$$\sum_{\mathbf{l}'j} \overset{(3)^{\alpha\beta\gamma}}{\phi}_{ijk}(\mathbf{0},\mathbf{l}',\mathbf{l}'') = 0, \tag{13}$$

which is named acoustic sum rule (ASR). It is straightforward that if Eq. 13 is fulfilled, the following as well

$$\sum_{\mathbf{l}'j\mathbf{l}''k} \overset{(3)^{\alpha\beta\gamma}}{\phi}_{ijk}(\mathbf{0},\mathbf{l}',\mathbf{l}'') = 0. \tag{14}$$

It can be proven that after centering, Eq. 14 is fulfilled but not Eq. 13. Therefore, the procedure is to first apply the centering and afterwards impose the ASR. For imposing the ASR, as explained in Ref. [3], first of all we calculate two quantities: $d_1 = \sum_{\mathbf{l}''k} \overset{(3)}{\phi}{}^{\alpha\beta\gamma}_{ijk}(\mathbf{0},\mathbf{l}',\mathbf{l}'')$ and $q_1 = \sum_{\mathbf{l}''k} |\overset{(3)}{\phi}{}^{\alpha\beta\gamma}_{ijk}(\mathbf{0},\mathbf{l}',\mathbf{l}'')|$ for every $\mathbf{l}'$, i, j, α, β and γ. Then we apply the operation $\overset{(3)}{\phi}{}^{\alpha\beta\gamma}_{ijk}(\mathbf{0},\mathbf{l}',\mathbf{l}'') = \overset{(3)}{\phi}{}^{\alpha\beta\gamma}_{ijk}(\mathbf{0},\mathbf{l}',\mathbf{l}'') - \frac{d_1}{q_1}|\overset{(3)}{\phi}{}^{\alpha\beta\gamma}_{ijk}(\mathbf{0},\mathbf{l}',\mathbf{l}'')|$ for every $\mathbf{l}''$ and k iteratively until the absolute value of the ASR is lower than a threshold value. In Figs. 7a,b we can see that the effect of imposing the ASR in this way barely affects the TOFCs, and the difference between the TOFCs with and without imposing the ASR is symmetric in positive and negative value.

In the case of the non-perturbative TOFCs we apply the same procedure in order to obtain interpolable TOFCs. As the non-perturbative TOFCs are calculated stochastically, we carefully check their convergence with respect to the number of configurations used to calculate them. As we can see in Fig. 8 the thermal conductivity is indeed converged to a value different from the perturbative result. In Figs. 7c,d we explicitly show the difference of the non-perturbative and perturbative TOFCs. The value of the non-perturbative TOFCs depends on the complex shape of the full $V(\mathbf{R})$ and temperature, contrary to the perturbative ones. In Fig. 9 we can see that in the calculations performed at lower temperatures in the PBE case, the non-perturbative TOFCs approach the perturbative limit as expected[11]. At higher temperatures, for the LDA calculations, the temperature dependence is weaker. The statistical uncertainty in the TOFCs is much smaller than the difference between perturbative and non-perturbative ones.

7 Thermal conductivity

In the SMA the thermal conductivity can be written as follows[3]:

$$\kappa_l^{\alpha\beta} = \frac{\hbar^2}{N_q \Omega K_B T^2} \sum_{\mathbf{q}\mu} c_\mu^\alpha(\mathbf{q}) c_\mu^\beta(\mathbf{q}) \omega_\mu^2(\mathbf{q}) n_B[\omega_\mu(\mathbf{q})](n_B[\omega_\mu(\mathbf{q})]+1)\tau_\mu(\mathbf{q}), \tag{15}$$

where Ω is the unit cell volume, K_B the Boltzmann constant, $c_\mu^\alpha(\mathbf{q})$ the Cartesian component α of the group velocity of normal mode $\mathbf{q}\mu$, $n_B[\omega_\mu(\mathbf{q})]$ the Bose-Einstein occupation of mode $\mathbf{q}\mu$ given by BTE and $\tau_\mu(\mathbf{q})$ the lifetime of mode $\mathbf{q}\mu$. As we can see from Eq. 15, the thermal conductivity is basically proportional to the squared group velocity and lifetime. Therefore, high group velocities and lifetimes yield a high thermal conductivity. The inverse lifetime (with $\gamma_\mu(\mathbf{q})$ half width at half maximum) is calculated as follows[3]:

$$\begin{aligned}\frac{1}{\tau_\mu(\mathbf{q})} = 2\gamma_\mu(\mathbf{q}) = \frac{\pi}{\hbar^2 N_q} \sum_{\mathbf{q}',\nu\eta} |\overset{(3)}{V}{}_{\mu\nu\eta}(\mathbf{q},\mathbf{q}',\mathbf{q}'')|^2 \\ \times [(1+n_B[\omega_\nu(\mathbf{q}')]+n_B[\omega_\eta(\mathbf{q}'')])\delta(\omega_\mu(\mathbf{q})-\omega_\nu(\mathbf{q}')-\omega_\eta(\mathbf{q}'')) \\ + 2(n_B[\omega_\nu(\mathbf{q}')]-n_B[\omega_\eta(\mathbf{q}'')])\delta(\omega_\mu(\mathbf{q})+\omega_\nu(\mathbf{q}')-\omega_\eta(\mathbf{q}''))],\end{aligned} \tag{16}$$

where $\overset{(3)}{V}_{\mu\nu\eta}(\mathbf{q},\mathbf{q}',\mathbf{q}'')$ is the TOFC matrix written in the space of the normal modes defined by the change of variable

$$\frac{\partial}{\partial X_\mu(\mathbf{q})} = \sum_a \sqrt{\frac{\hbar}{2M_a\omega_\mu(\mathbf{q})}} e^a_\mu(\mathbf{q}) \frac{\partial}{\partial u_a(\mathbf{q})} \tag{17}$$

and fulfilling $\mathbf{q}+\mathbf{q}'+\mathbf{q}'' = \mathbf{G}$, $\mathbf{G}$ being a reciprocal lattice vector. $\omega_\mu(\mathbf{q})$ is the energy of phonon $\mathbf{q}\mu$.

In Fig. 10 we plot the group velocity, linewidth, cumulative lattice thermal conductivity ($\kappa_l^c(\omega) = \int_0^\omega \kappa(\omega)d\omega$) and the phonon density of states (PDOS). As we see in Fig. 10a, due to the layered structure of the system, the group velocity is much lower in the out-of-plane direction x, leading to a reduced thermal conductivity. The two in-plane directions show very similar group velocities, as we would expect in this high symmetry phase. Interestingly, we can see in Fig. 10b that the non-perturbative linewidth has a similar dispersion to the perturbative one, however, it is homogeneously bigger in the whole frequency range. In agreement with the spectral function, this makes clear the need for a non-perturbative treatment of SnSe and yields a much lower thermal conductivity as we can see in Fig. 10c. From Fig. 10c we can also extract that almost the entire contribution to the thermal conductivity is coming from vibrational modes with frequency smaller than 100 cm^{-1}. Furthermore, more than 50% of the thermal conductivity is coming from the acoustic modes ($\omega < 75$ cm^1) which, looking at the phonon density of states in Fig. 10d, is mainly coming from the vibrations of Sn atoms. The rest of the in-plane thermal conductivity is coming from the Sn and Se vibrations at around 90 cm^{-1}. The situation is different for the out-of-plane component due to its very low group velocity in the $50-150$ cm^{-1} frequency range. The rest of its contribution is coming from high energy modes where group velocities are higher. The contribution of the optical modes is strongly suppressed by the large phonon linewidths, which are a consequence of the strong anharmonicity of this compound. The contribution of the acoustic modes is particularly low, which ensures a low κ_l, specially because they can strongly scatter among themselves and with the Γ_1 mode. Therefore, the strongly anharmonic modes (Γ_1, Γ_2) provide an important scattering channel for lowering the thermal conductivity and making SnSe a very good thermoelectric material.

Here we compare our thermal conductivity results with the theoretical result by Skelton et al. [12] in Fig. 11. We can see that the different calculations agree qualitatively but quantitatively their values are much lower. Considering that in that work only the frequencies of the Γ_1 and Y_1 modes are renormalized, the comparison is not clear. Indeed, as shown in the main text, all phonon modes across the Brillouin zone suffer from a strong anharmonic renormalization, which affects the calculation of the thermal conductivity.

Finally, we compare the theoretical thermal conductivities for the low and high temperature phases. Our goal is to determine how much the small atomic displacement associated to the second-order phase transition affects the thermal conductivity of the *Pnma* phase. To address that we calculate the thermal conductivities of the *Pnma* phase in a $1\times2\times2$ supercell and, in order to make the calculations fully comparable, we compare it with the thermal conductivity calculated for the *Cmcm* phase in the same $1\times2\times2$ conventional lattice. In both cases we use SSCHA phonon frequencies and non-perturbative TOFCs calculated within the LDA. In the *Pnma* calculations SSCHA phonons and non-perturbative force-constants are calculated at 500 K, just below the theoretical transition, and in the *Cmcm* at 700 K, just above the transition. As we can see in Fig. 12, the thermal conductivities are very similar, remarking

that the small atomic displacement of the *Pnma* phase close to the transition barely affects the thermal conductivity. It is true however that experimentally[13] and theoretically[12] the values for the *Pnma* phase are a slightly higher, in agreement with our calculations. Anyhow, the difference between the two phases close to the phase transition is considerably smaller than the effect of anisotropy or non-perturbative calculations.

Comparing the *Cmcm* results of Fig. 12 with those of Fig. 5 of the main text, we can see that the thermal conductivities are considerably lower using a $1 \times 2 \times 2$ conventional cell. This shows, that the $1 \times 2 \times 2$ conventional cell calculation is underconverged for the *Cmcm* phase, and probably as well for the *Pnma* phase. Performing calculations on a larger supercell for the low-symmetry phase would require a non-affordable computational effort. This makes that, even if the comparison between the two phases in Fig. 12 is fair, the absolute values in this figure should be taken with care. On the contrary, as shown in Fig. 1, the thermal conductivity of the *Cmcm* on the $2 \times 2 \times 2$ primitive supercell is converged with respect to the $4 \times 4 \times 4$ calculation in a 10%. The differences between the results in Fig. 12 with those of Fig. 5 of the main text are thus mainly related to the different q-point sampling used.

References

[1] Paolo Giannozzi, Stefano Baroni, Nicola Bonini, Matteo Calandra, Roberto Car, Carlo Cavazzoni, Davide Ceresoli, Guido L Chiarotti, Matteo Cococcioni, Ismaila Dabo, et al. Quantum espresso: a modular and open-source software project for quantum simulations of materials. *Journal of physics: Condensed matter*, 21(39):395502, 2009.

[2] Stefano Baroni, Stefano De Gironcoli, Andrea Dal Corso, and Paolo Giannozzi. Phonons and related crystal properties from density-functional perturbation theory. *Reviews of Modern Physics*, 73(2):515, 2001.

[3] Lorenzo Paulatto, Francesco Mauri, and Michele Lazzeri. Anharmonic properties from a generalized third-order ab initio approach: Theory and applications to graphite and graphene. *Physical Review B*, 87(21):214303, 2013.

[4] Wu Li, Jesús Carrete, Nebil A. Katcho, and Natalio Mingo. Shengbte. *Comp. Phys. Commun.*, 185:1747–1758, 2014.

[5] John P Perdew, Kieron Burke, and Matthias Ernzerhof. Generalized gradient approximation made simple. *Physical review letters*, 77(18):3865, 1996.

[6] G Kresse and J Hafner. Norm-conserving and ultrasoft pseudopotentials for first-row and transition elements. *Journal of Physics: Condensed Matter*, 6(40):8245, 1994.

[7] Peter E Blöchl. Projector augmented-wave method. *Physical review B*, 50(24):17953, 1994.

[8] Norman Troullier and José Luís Martins. Efficient pseudopotentials for plane-wave calculations. *Physical review B*, 43(3):1993, 1991.

[9] Giorgia Fugallo, Michele Lazzeri, Lorenzo Paulatto, and Francesco Mauri. Ab initio variational approach for evaluating lattice thermal conductivity. *Physical Review B*, 88(4):045430, 2013.

[10] Antoine Dewandre, Olle Hellman, Sandip Bhattacharya, Aldo H Romero, Georg KH Madsen, and Matthieu J Verstraete. Two-step phase transition in snse and the origins of its high power factor from first principles. *Physical review letters*, 117(27):276601, 2016.

[11] Raffaello Bianco, Ion Errea, Lorenzo Paulatto, Matteo Calandra, and Francesco Mauri. Second-order structural phase transitions, free energy curvature, and temperature-dependent anharmonic phonons in the self-consistent harmonic approximation: Theory and stochastic implementation. *Physical Review B*, 96(1):014111, 2017.

[12] Jonathan M Skelton, Lee A Burton, Stephen C Parker, Aron Walsh, Chang-Eun Kim, Aloysius Soon, John Buckeridge, Alexey A Sokol, C Richard A Catlow, Atsushi Togo, et al. Anharmonicity in the high-temperature c m c m phase of snse: Soft modes and three-phonon interactions. *Physical review letters*, 117(7):075502, 2016.

[13] Li-Dong Zhao, Shih-Han Lo, Yongsheng Zhang, Hui Sun, Gangjian Tan, Ctirad Uher, Christopher Wolverton, Vinayak P Dravid, and Mercouri G Kanatzidis. Ultralow thermal conductivity and high thermoelectric figure of merit in snse crystals. *Nature*, 508(7496):373–377, 2014.

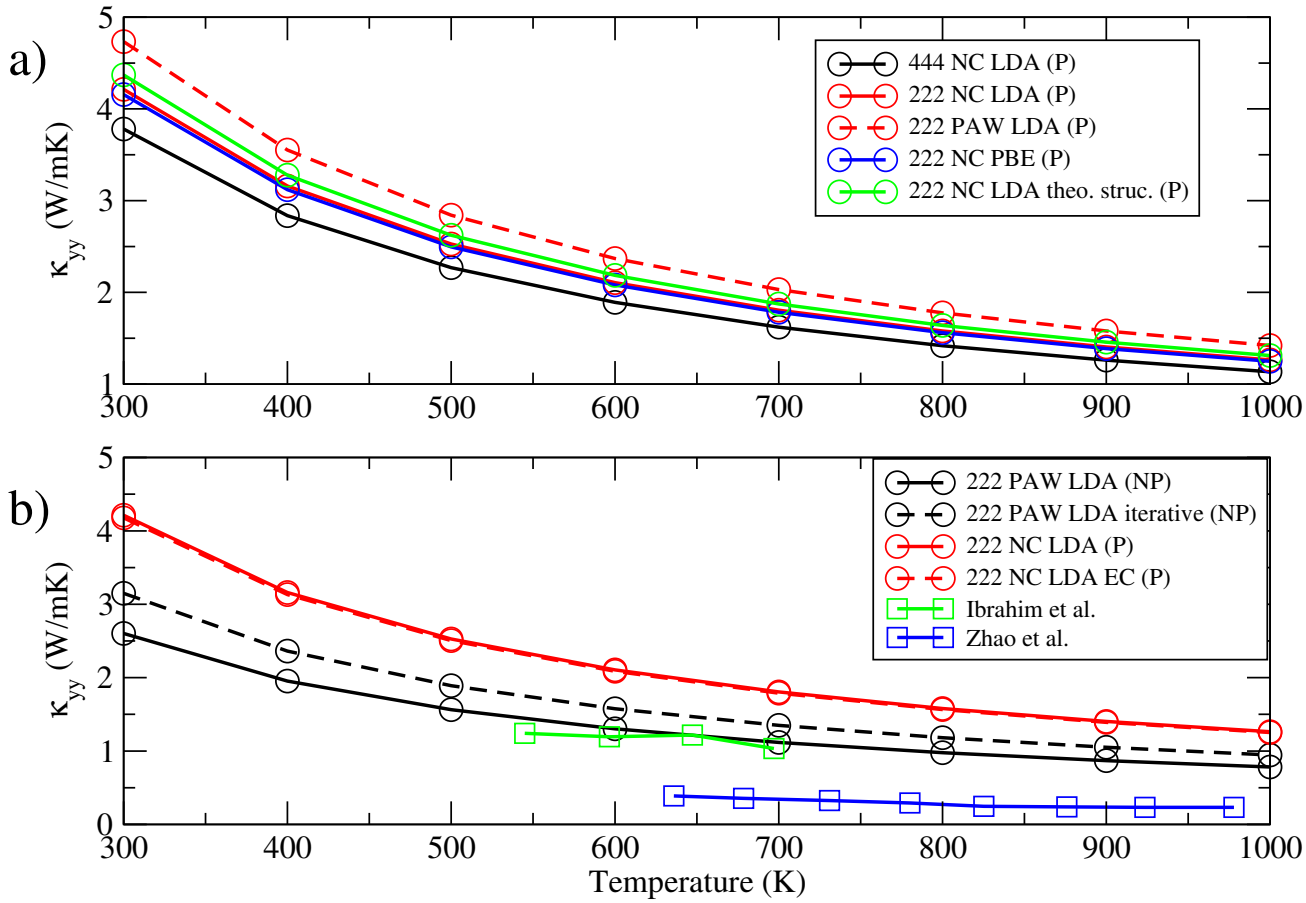

Figure 1: κ_{yy} component of the lattice thermal conductivity within different approximations (Perturbative (P) and non-perturbative (NP)), parameters, structures and pseudopotentials (see legends). a) Thermal conductivity of SnSe using norm-conserving (NC) LDA pseudopotential and a $2\times2\times2$ supercell (solid red), NC LDA pseudopotential and a $4\times4\times4$ supercell (black), PAW LDA pseudopotential with a $2\times2\times2$ supercell (dashed red), NC PBE pseudopotential with a $2\times2\times2$ supercell (solid blue) and NC LDA pseudopotential with a $2\times2\times2$ supercell in the fully relaxed structure (solid green). b) Thermal conductivity of SnSe using NC LDA pseudopotential and a $2\times2\times2$ supercell (solid red), NC LDA pseudopotential including effective charges (EC) in a $2\times2\times2$ supercell (dashed red), non-perturbative (NP) PAW LDA calculation using a $2\times2\times2$ supercell and PAW LDA calculation using the iterative method in a $2\times2\times2$ supercell. Experimental points are shown as squares. All calculations are done using the experimental structure but the green data in a). In the experimental lattice we use the $\tilde{\Omega}_\mu$ phonons at 700 K in LDA and 500 K in PBE. For the calculation in the theoretical structure we use the $\tilde{\Omega}_\mu$ phonons at 400 K. The other Cartesian components show a similar behavior.

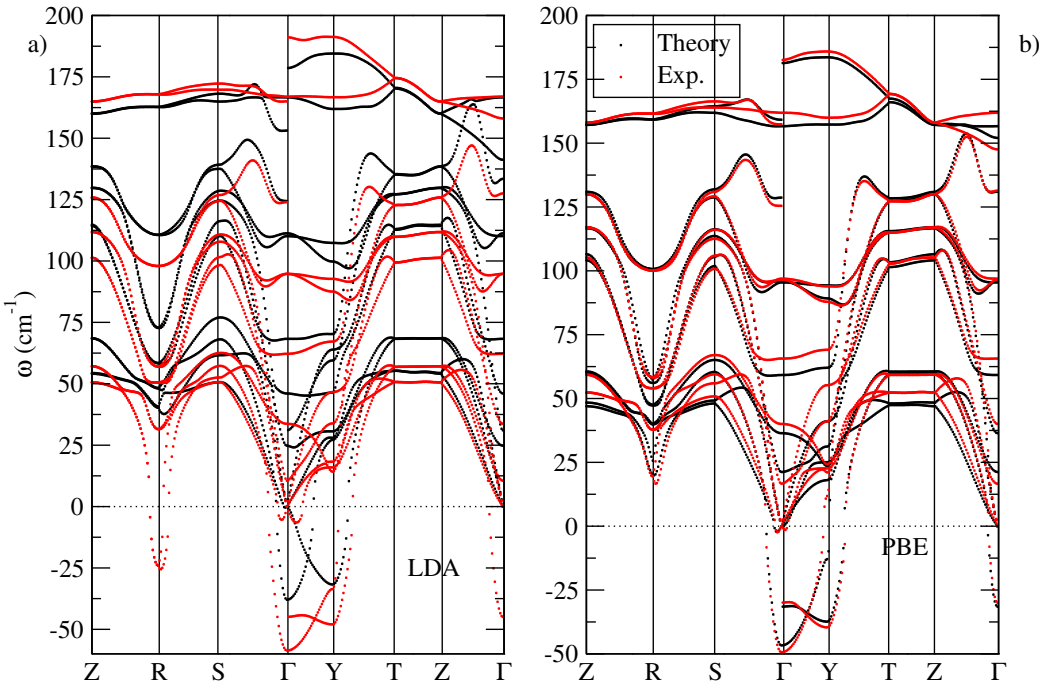

Figure 2: a) LDA harmonic phonon spectra in the theoretical and experimental structures. b) The same as a) within PBE. The LO-TO splitting is included in the calculations.

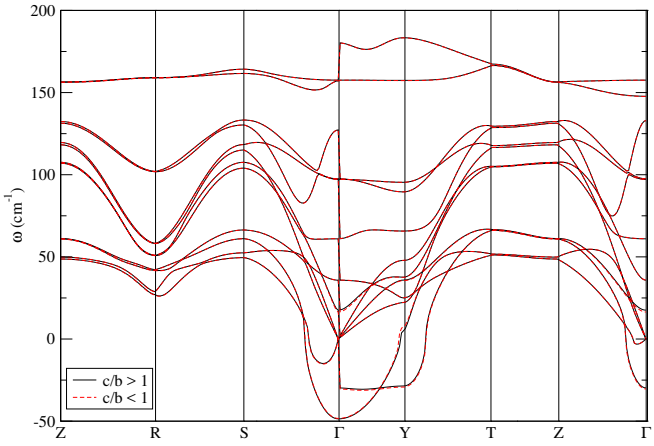

Figure 3: PBE harmonic phonon spectra with the following lattice parameters: $a = 22.492$, $b = 8.094$ and $c = 8.090$ (in Bohr units) (red) in one case and exchanging b and c (black) in the other. We have done the calculation in a $2 \times 2 \times 2$ supercell and Fourier interpolated to plot the spectrum. The LO-TO splitting is included in the calculations.

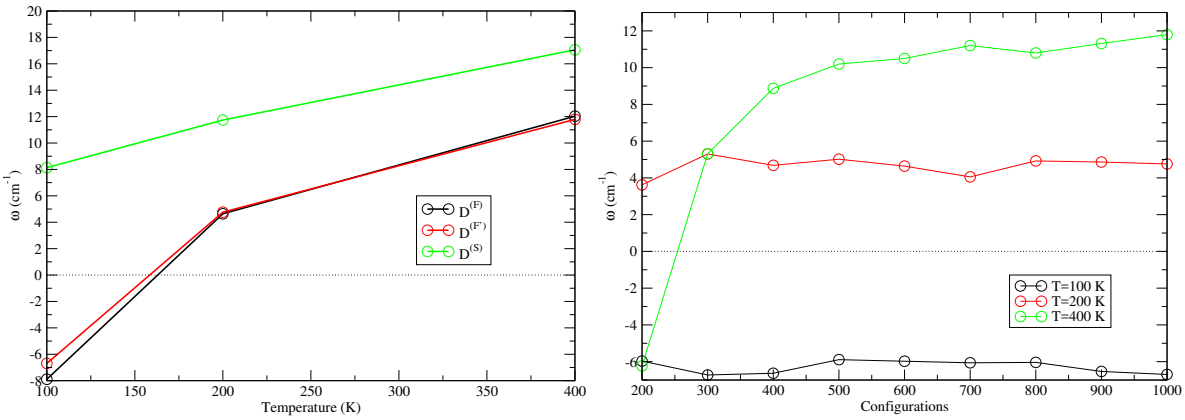

Figure 4: Left panel: Frequency of the mode Y_1 as a function of temperature within LDA in the theoretical structure within different approximations. The black circles corresponds to $\mathbf{D}^{(F)}$, the green ones to $\mathbf{D}^{(S)}$ and the red ones to $\mathbf{D}^{(F')}$, which is the same as $\mathbf{D}^{(F)}$ with $\overset{(4)}{\mathbf{\Phi}} = 0$. Right panel: We show the convergence of the frequency calculated from $D^{(F')}$ with respect to the number of stochastic configurations used for the SSCHA at different temperatures. The convergence is the same for $D^{(F)}$.

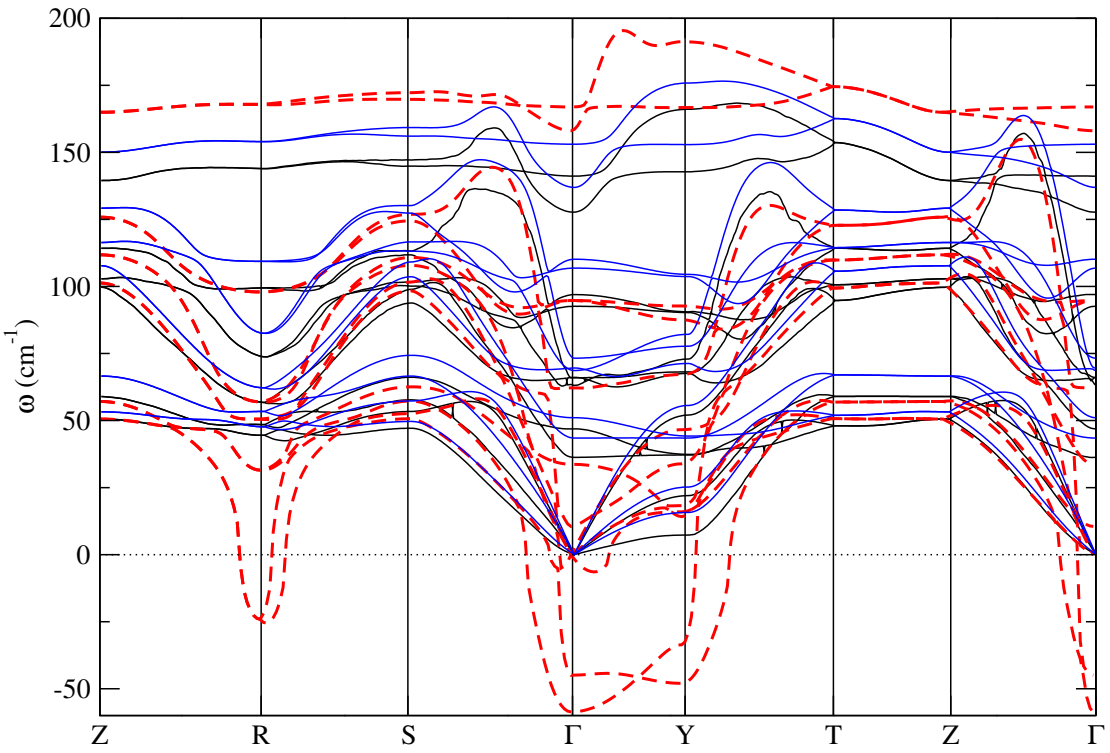

Figure 5: Harmonic (dashed red), $\tilde{\Omega}_\mu$ (blue) and Ω_μ (black) phonon spectra. Anharmonic phonons are calculated at 800 K within LDA in the experimental lattice.

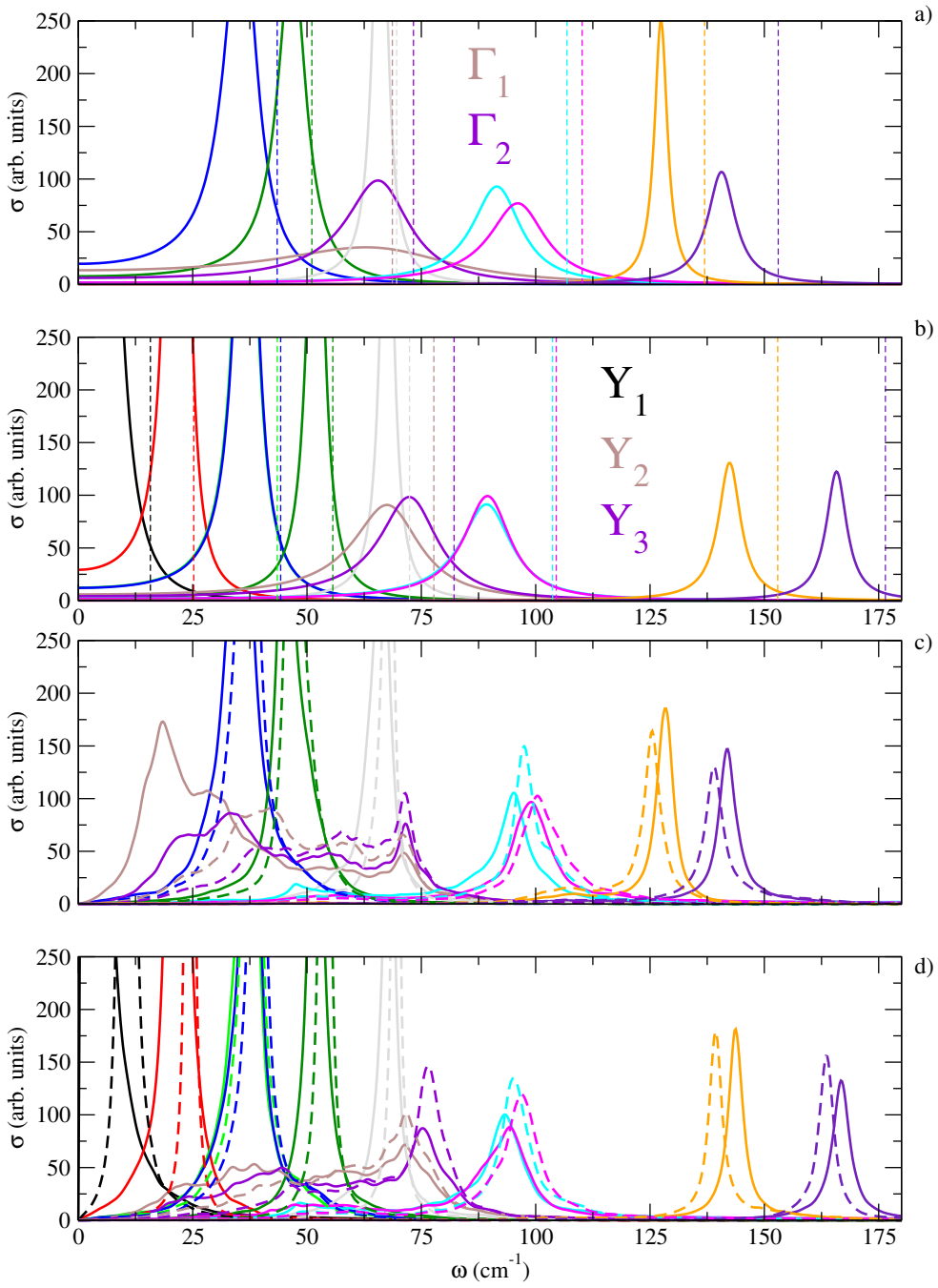

Figure 6: a) Non-perturbative spectral functions calculated in the Lorentzian approximation at the Γ point. b) The same as a) at the point Y. Dashed vertical lines correspond to $\tilde{\Omega}_\mu$ frequencies. c) Non-perturbative (solid lines) and perturbative (dashed lines) spectral functions calculated at the Γ point. d) The same as c) at the point Y. The calculations are done using $\tilde{\Omega}_\mu$ SSCHA frequencies at 800 K within LDA in the experimental structure. Non-perturbative calculations are done with TOFCs at 800 K.

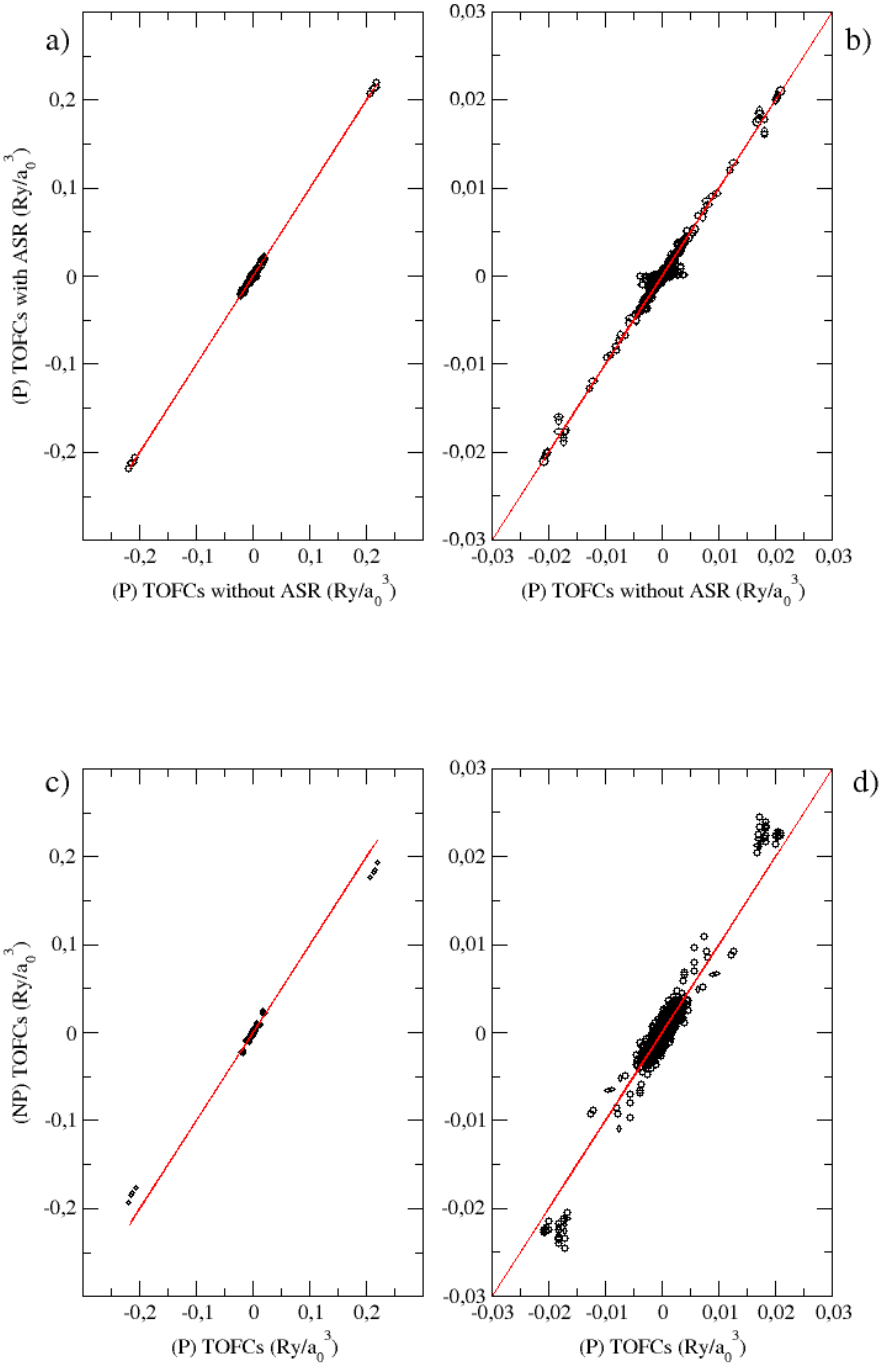

Figure 7: a) The value of the perturbative TOFCs after applying the acoustic sum rule as a function of the value without applying it. We include a $y = x$ line for comparison. b) A zoom of panel a). c) The value of the non-perturbative TOFCs without ASR as a function of the value of the perturbartive TOFCs without ASR. We include a $y = x$ line for comparison. d) A zoom of panel c). All the calculations are done within LDA in the experimental structure at 800 K.

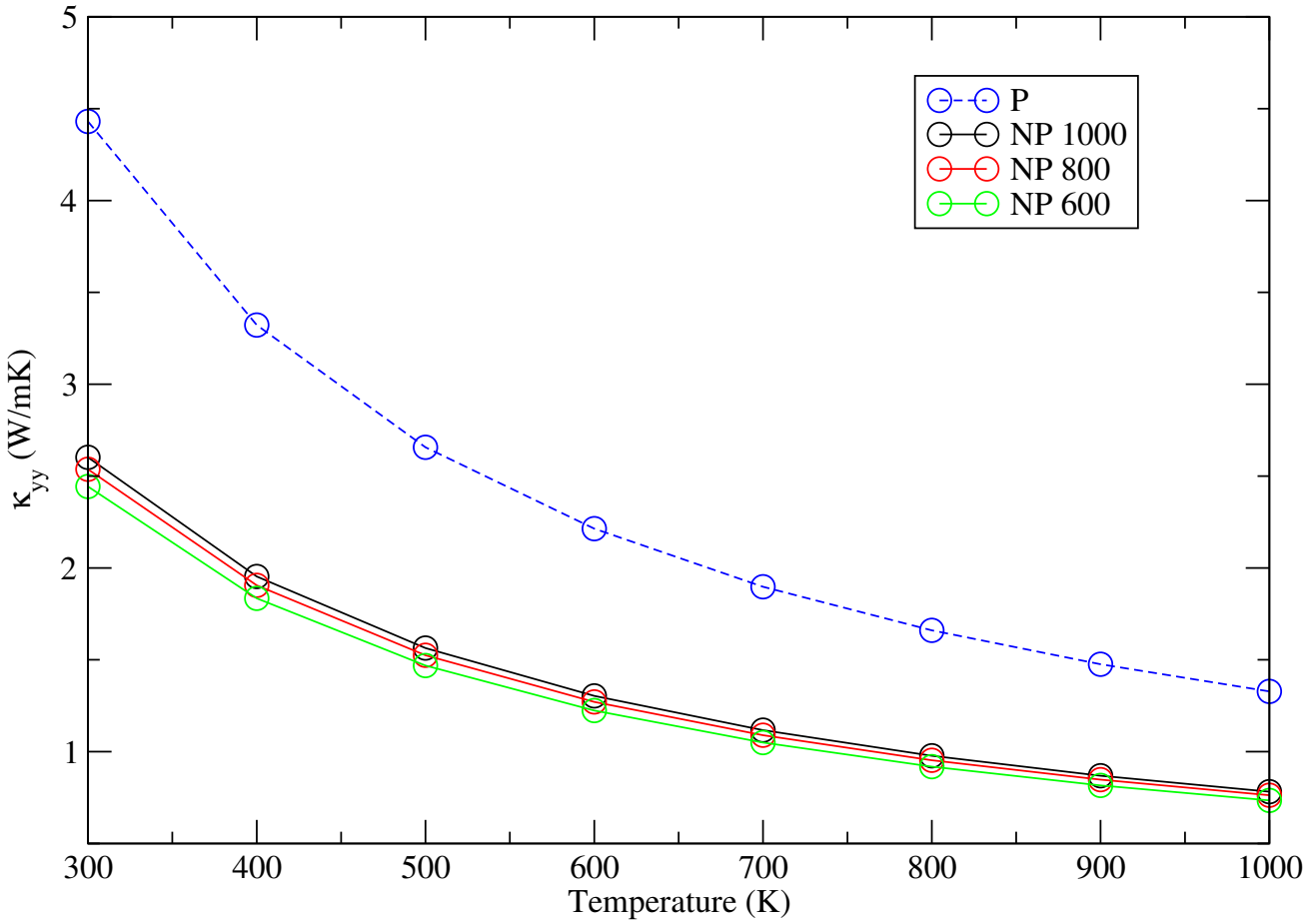

Figure 8: κ_{yy} component of the thermal conductivity (other components show a similar behavior). Solid lines correspond to calculations with different number of stochastic configurations (numbers in the legends). The dashed line corresponds to the perturbative (P) calculation. All the calculations are done within LDA in the experimental structure at 800 K.

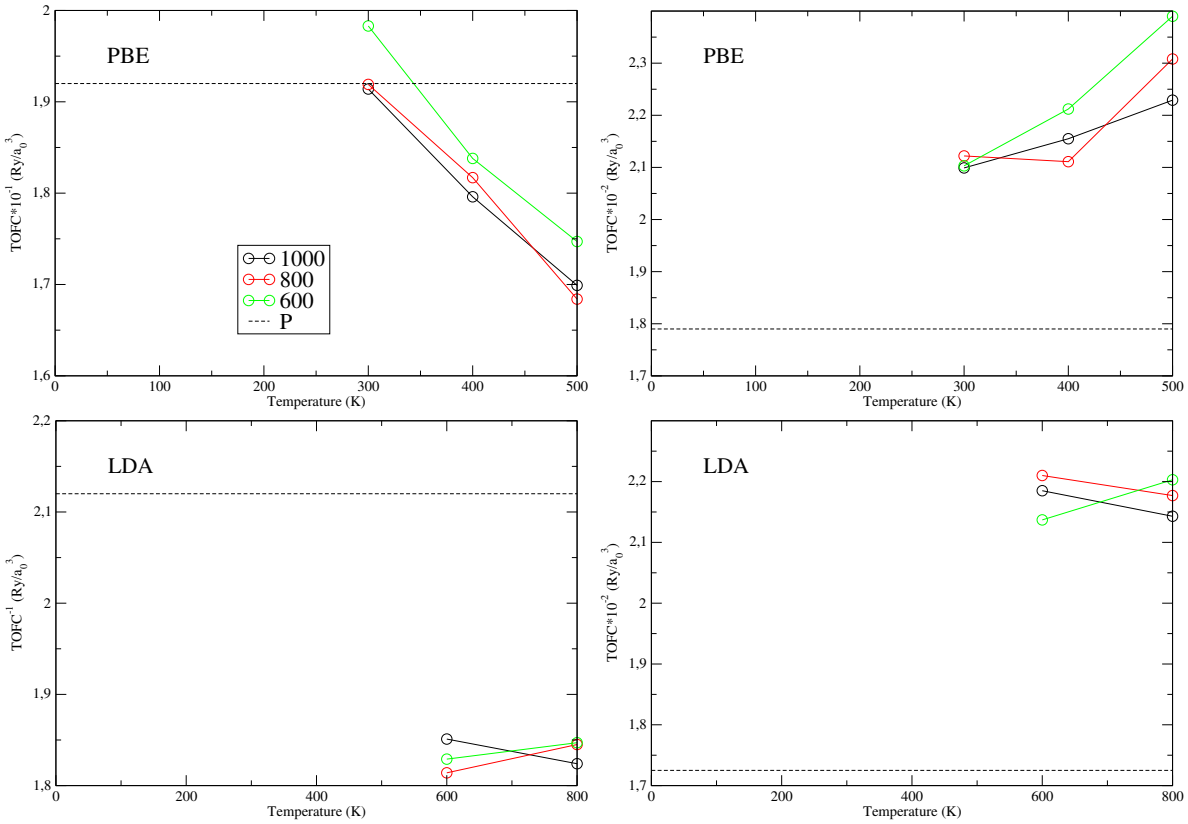

Figure 9: Two different TOFCs of two different orders of magnitude calculated within PBE and LDA at the experimental structure as a function of temperature. Dashed lines correspond to perturbative calculations, which are independent of temperature. The value of the non-perturbative TOFCs obtained with different amount of stochastic configurations is shown.

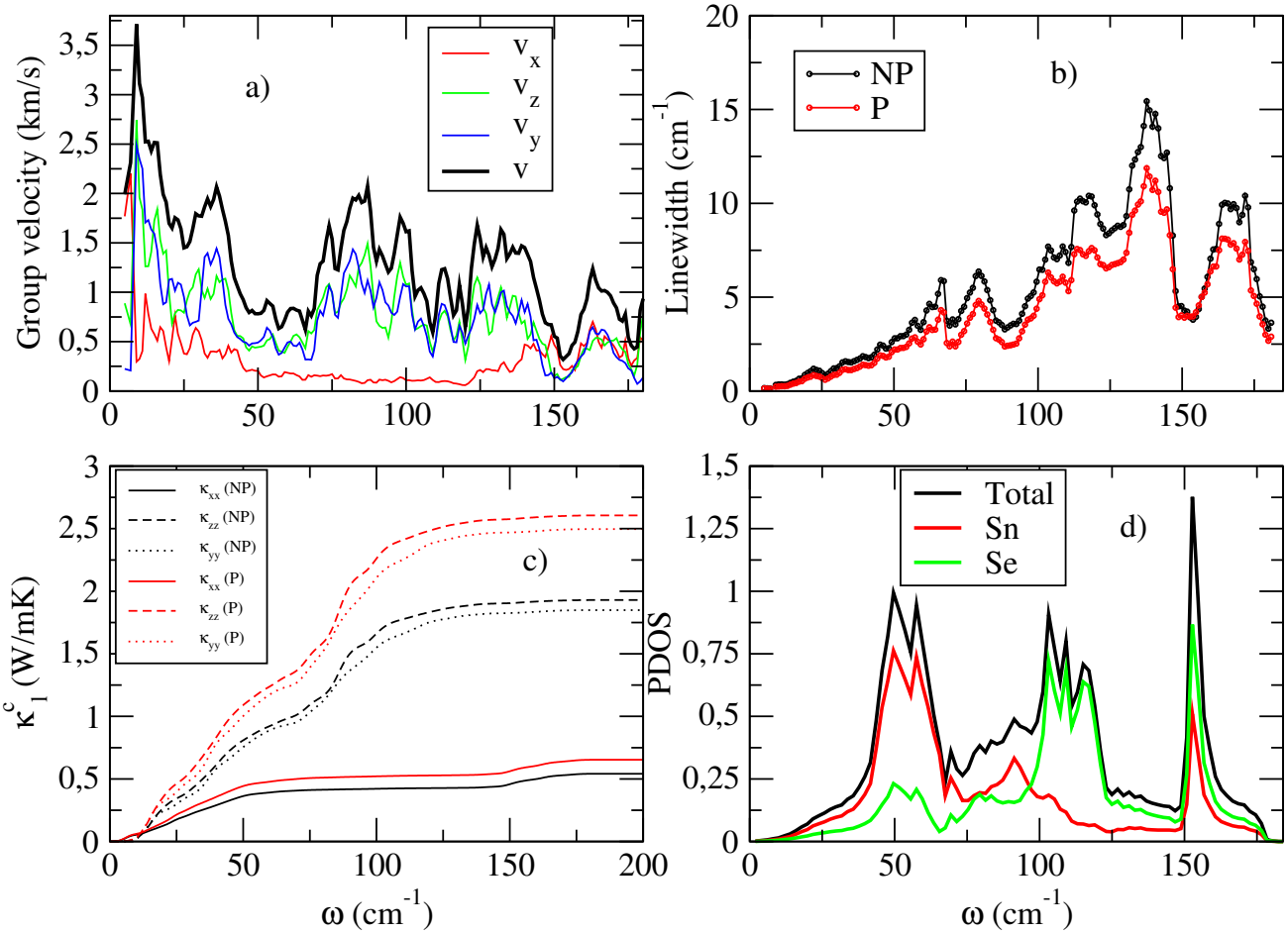

Figure 10: a) Absolute value of the phonon group velocity and absolute values of the group velocity Cartesian components. b) Average linewidth as a function of frequency for perturbative (P) (red) and non-perturbative (NP) (black) approaches. c) Diagonal components of the cumulative thermal conductivity as a function of frequency at 800 K for perturbative (P) (red) and non-perturbative (NP) (black) approaches. d) Phonon density of states and the projections in Sn and Se atoms. The calculations are done within LDA in the experimental structure using $\tilde{\Omega}_\mu$ frequencies and non-perturbative TOFCs at 800 K.

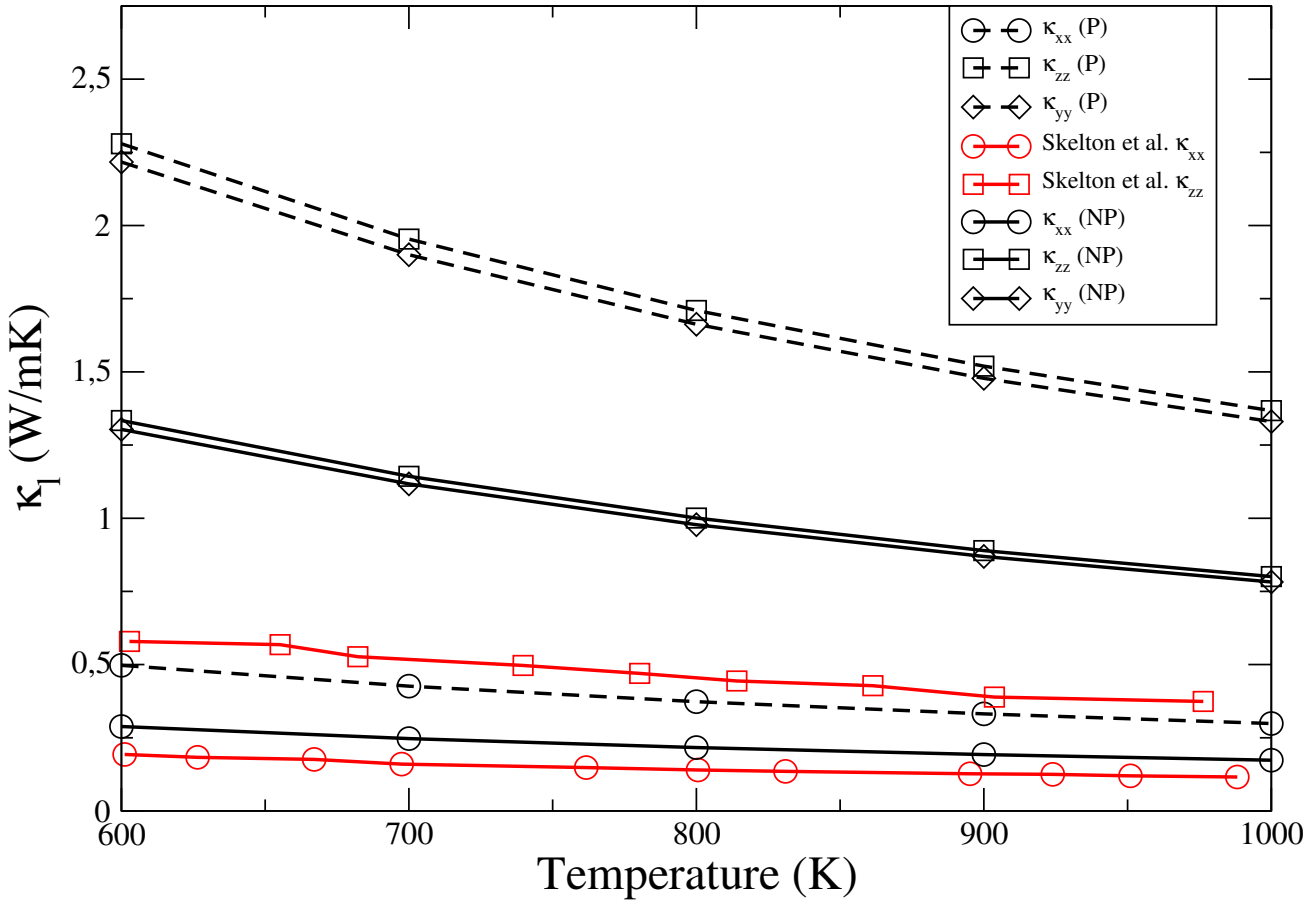

Figure 11: Perturbatve (P) and non-perturbative (NP) thermal conductivity within LDA with $\tilde{\Omega}_\mu$ at 800 K in the experimental structure compared to the results by skelton et al. From the data of Skelton et al. we see that $\kappa_{yy} \sim \kappa_{zz}$, that is why we only show κ_{zz}.

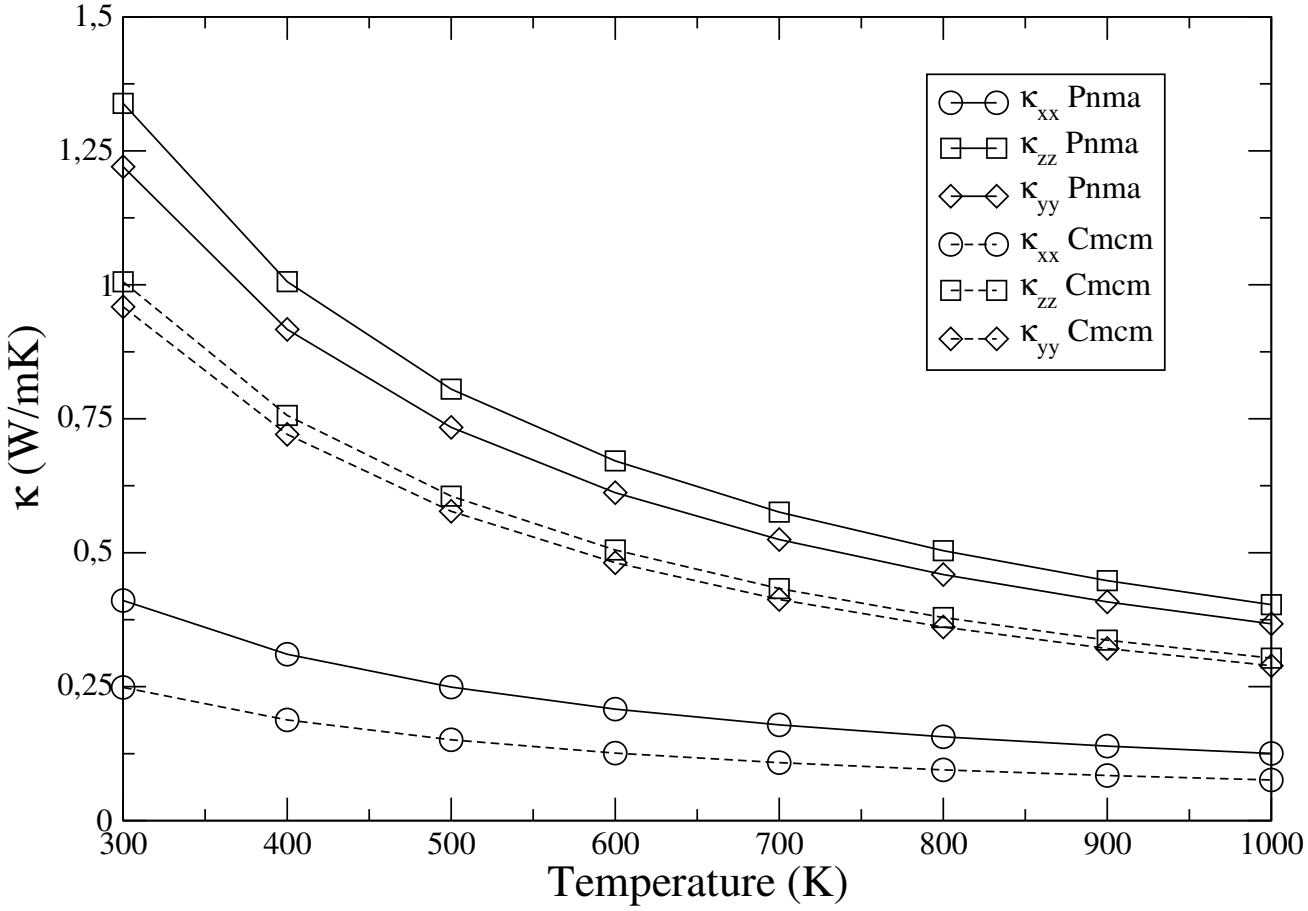

Figure 12: Non-perturbative LDA lattice thermal conductivity of the Pnma (solid) and Cmcm (dashed) phases.